


Article

Optimizing Smoke and Plume Rise Modeling Approaches at Local Scales

Derek V. Mallia ^{1,*}, Adam K. Kochanski ¹, Shawn P. Urbanski ² and John C. Lin ¹ 

¹ Department of Atmospheric Sciences, University of Utah, Salt Lake City, UT 84112, USA; adam.kochanski@utah.edu (A.K.K.); John.Lin@utah.edu (J.C.L.)

² Missoula Fire Science Laboratory, U.S. Forest Service, Missoula, MT 59808, USA; surbanski@fs.fed.us

* Correspondence: Derek.Mallia@utah.edu

Received: 9 April 2018; Accepted: 25 April 2018; Published: 1 May 2018



Abstract: Heating from wildfires adds buoyancy to the overlying air, often producing plumes that vertically distribute fire emissions throughout the atmospheric column over the fire. The height of the rising wildfire plume is a complex function of the size of the wildfire, fire heat flux, plume geometry, and atmospheric conditions, which can make simulating plume rises difficult with coarser-scale atmospheric models. To determine the altitude of fire emission injection, several plume rise parameterizations have been developed in an effort estimate the height of the wildfire plume rise. Previous work has indicated the performance of these plume rise parameterizations has generally been mixed when validated against satellite observations. However, it is often difficult to evaluate the performance of plume rise parameterizations due to the significant uncertainties associated with fire input parameters such as fire heat fluxes and area. In order to reduce the uncertainties of fire input parameters, we applied an atmospheric modeling framework with different plume rise parameterizations to a well constrained prescribed burn, as part of the RxCADRE field experiment. Initial results found that the model was unable to reasonably replicate downwind smoke for cases when fire emissions were emitted at the surface and released at the top of the plume. However, when fire emissions were distributed below the plume top following a Gaussian distribution, model results were significantly improved.

Keywords: smoke modeling; fires; fire plume rise; atmospheric modeling

1. Introduction

Research has shown that fires are responsible for emitting a significant amount of aerosols (PM_{2.5} and PM₁₀) and trace gases (CO, CO₂, and CH₄) into Earth's atmosphere [1]. CO₂ and CH₄ are greenhouse gases responsible for climate change [2] while CO, PM_{2.5}, and PM₁₀ are criteria pollutants regulated by the U.S. Environmental Protection Agency (EPA). Aerosols can have significant impacts on radiative forcing and are considered one of the largest sources of uncertainty in climate model projections [3–5].

Aerosols from wildfires can have significant impacts on air quality and human health. Depending on the size of the fire, large amounts of trace gases and aerosols can be advected over large distances (>1000-km) downwind of the fire [6]. As a result, smoke from wildfires can often have local and regional impacts on air quality and visibility. Across the western USA, wildfires have already been increasing in size and frequency since the mid-1980s, with these trends being linked to warmer temperatures, which have resulted in earlier snowmelt [7]. Impacts from wildfire smoke are projected to worsen through the end the 21st century as the number of large fires increases as a result of climate change [8–10].

The height of the wildfire plume rise can have significant impacts on the downwind transport of smoke. Heating from wildfires adds buoyancy to the overlying air, often producing plumes that vertically distribute fire emissions throughout the atmospheric column over the fire. The height that emissions reach, which is commonly referred to as the wildfire plume height, is often a complex function of the size of the wildfire, fire heat flux, and the atmosphere's environmental conditions [11]. As a result, plume heights can vary significantly, ranging from a few hundred meters to altitudes that extend into the lower stratosphere for the most extreme pyro-convection [12,13]. Generally, the majority of wildfire plume rises remain confined within the planetary boundary layer (PBL); however, it is estimated that approximately 5–18% of all wildfire plumes reach the free troposphere [14,15].

For example, smoke that is primarily injected within the PBL generally becomes well mixed throughout the depth of the PBL and remains close to the emission source as a result of weaker near-surface winds. In addition, chemically active smoke pollutants such as particulate matter have a much shorter lifetime within the PBL due to wet and dry deposition [13]. However, smoke that is lofted into the free troposphere will advect farther downwind from the fire and can result in regional and global impacts [16].

Various plume rise techniques have been developed over the years in an effort to determine the injection height of wildfire emissions within atmospheric and chemical transport models [13]. These plume rise techniques range from simple empirical-based schemes such as Briggs, Sofiev, and DAYSMOKE [17–19] to more sophisticated prognostic 1-D parcel models that include cloud microphysics and entrainment [20]. Even more advanced modeling frameworks exist such as the Weather Research and Forecast model–fire-spread module (WRF–SFIRE) [21], which has the ability to explicitly resolve fire spread and fire plume dynamics by coupling the Weather Research and Forecast model (WRF) [22] with a fire-spread module (SFIRE). Coupled models such as WRF–SFIRE are primarily intended to be used in a forecast mode. WRF–SFIRE computes the spread of the fire, and uses this information to estimate the heat and emission fluxes [23]. The rate of spread and the emission estimates within WRF–SFIRE are associated with hard to quantify uncertainties. Thus, it is often difficult to apply models such as WRF–SFIRE to hindcast applications such as constraining emissions or estimating contributions of particular fires to the concentrations at a point of interest.

Research has been carried out in an effort to validate existing plume rise formulations against observations [11,16,19,24]. Modeled plume rise heights using the Freitas model were compared to a subset of satellite-based Multiangle Imaging Spectroradiometer (MISR) observations [11]. Results from this study concluded that the Freitas model [20] was unable to reliably predict the height of a plume ($R \sim 0.3$), with plume height errors being attributed to uncertainties in the fire input parameters (fire heat flux, fire area) and the entrainment parameterization [11]. Validation studies have also been carried out for the empirical-based methodologies, which found that the Sofiev model had a significant negative bias while the Briggs model only had a correlation of $R < 0.2$ when compared to a subset of MISR estimated plume rises [19,25].

These recent studies have underscored the fact that research is still needed to reduce the uncertainties associated with existing plume rise models. For example, it is unclear whether uncertainties in modeled plume rise heights are directly associated with plume rise parameterizations or fire input parameters, or both. In an effort to constrain potential sources of model errors, various studies have recommended the testing of plume rise models for case studies where there is an abundance of field measurements that can adequately resolve the spatiotemporal frequency of wildfire characteristics [11,25,26]. Furthermore, there has been even less research that focuses on modeling the vertical distribution of smoke emissions as a result of the wildfire plume rise and the subsequent downwind transport of smoke at local and regional scales.

Following the recommendations of previous work, we applied classic plume rise modeling approaches to a well-constrained prescribed burn during the Prescribed Fire Combustion and Atmospheric Dynamics Research Experiment (RxCADRE). An atmospheric transport model was used simulate smoke transport with modeled smoke concentrations being validated against aircraft

measurements (Section 2). For this case study, we determined the optimal model configuration needed to compute the wildfire plume rise and downwind transport of smoke at local scales for the RxCADRE experiment. From this, we hope that the optimal model configuration identified here can improve plume rise modeling for general wildfire smoke modeling applications in the future.

2. Methodology

A series of prescribed burns were carried out at Eglin Air Force Base, FL during the fall of 2012 in an effort to better understand fire behavior and fire-atmosphere interactions [27–30] (Figure 1). The largest operational prescribed burn (L2F) occurred on 11 November 2012 between 1804 and 2059 UTC, which consisted of a sub-forest-canopy fire over a 151 ha plot (Figure 2a). The L2F operational burn was ignited along 3 simultaneously generated firing lines, which transected the L2F plot from the northeast to southwest (Figure 3). A number of measurements such as fuel characteristics, fuel loadings and consumption, airborne fire radiative power (FRP), and smoke dispersion were collected to better understand fire emissions and the downwind dispersion of smoke (Figure 2b).

Prevailing winds during the L2F prescribed burn were out of the southeast ($\sim 130^\circ$) as a result of a surface high located to the northeast of North Carolina and a trough approaching from the northwest (Figure 4). Prior to the burn at 1525 UTC, a morning stable layer at 600-mASL was present (Figure 5a) with a moist layer extending from the surface to 2-km as a result of southeasterly winds drawing moisture from the Gulf of Mexico. By the end of the L2F experiment, convective mixing from daytime heating eroded the cap aloft, resulting in an atmospheric profile that was well-mixed through ~ 1600 -m (Figure 5b). Winds throughout the PBL were consistently out of the southeast at 130 – 140° .

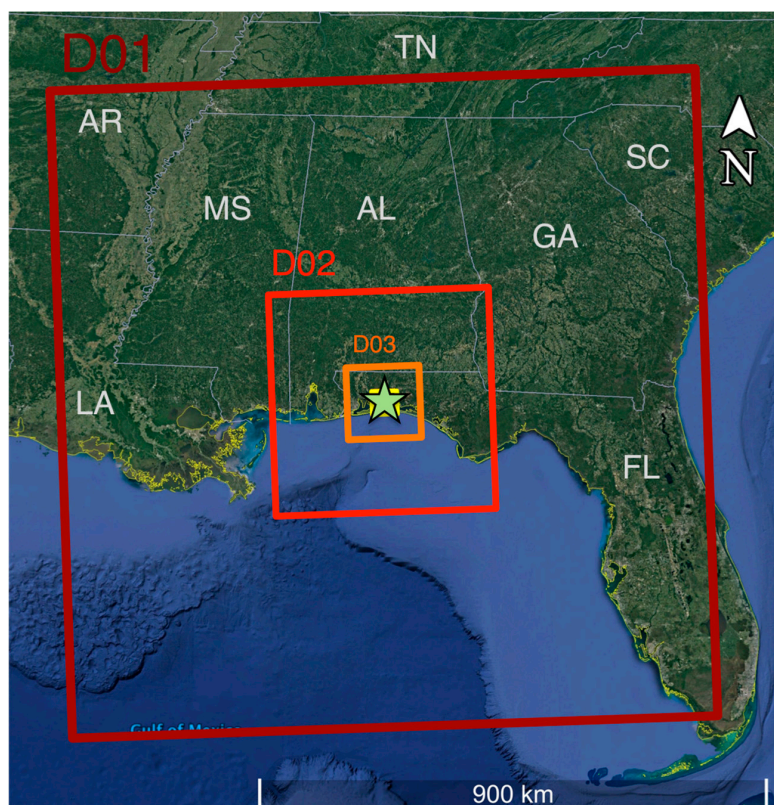


Figure 1. The Weather Research and Forecast (WRF) domain used for the RxCADRE L2F experiment. The horizontal grid spacing for each domain is as follows: 12-km (D01), 4-km (D02), and 1333-km (D03). The innermost domain (yellow) represents D04, which has a grid spacing of 0.444-km. Light green star denotes the location of Eglin Air Force Base. Map data: Google, DigitalGlobe.

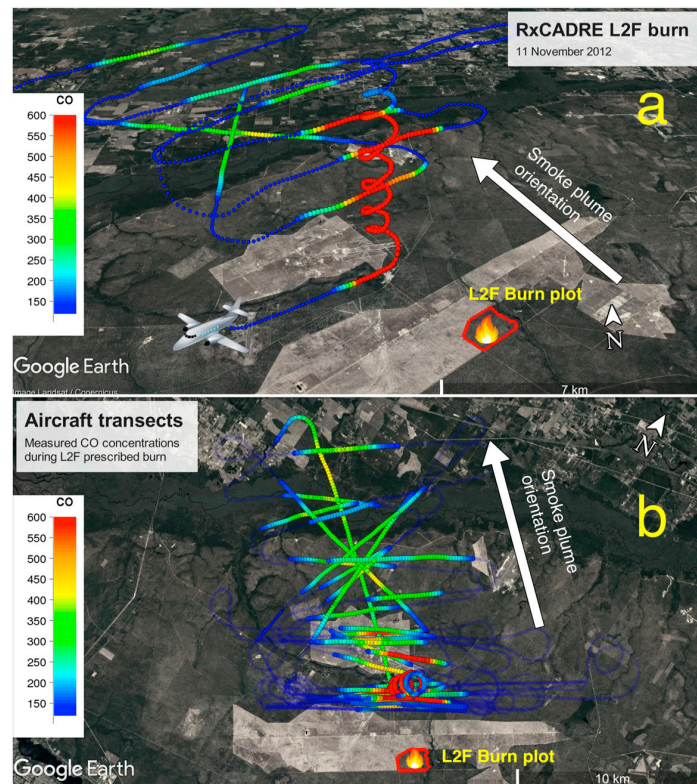


Figure 2. (a) 3-D image of the RxCADRE L2F prescribed on 11 November 2012. The L2F burn plot is outlined in red, and colored circles indicate aircraft measured CO (ppb) from 17:42–20:50 UTC. (b) Overhead (2-D) view of the same aircraft measurements in (a), but for 1742 through 2050 UTC. In addition, background concentrations (<120 ppb) have a transparency of 50% in order to highlight smoke enhanced smoke concentrations.

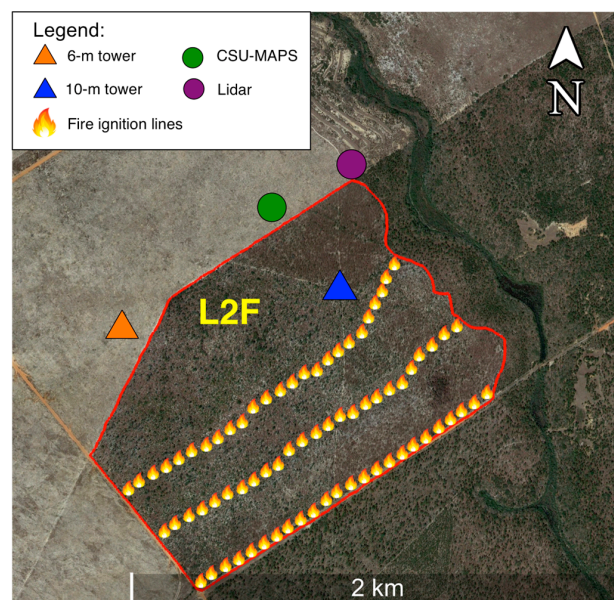


Figure 3. Meteorological measurement and ignition line locations during the L2F operational burn. The California State University–Mobile Atmospheric Profiling System (CSU–MAPS) is abbreviated for the California State University–Mobile Atmospheric Profiling System. Map data: Google, DigitalGlobe.

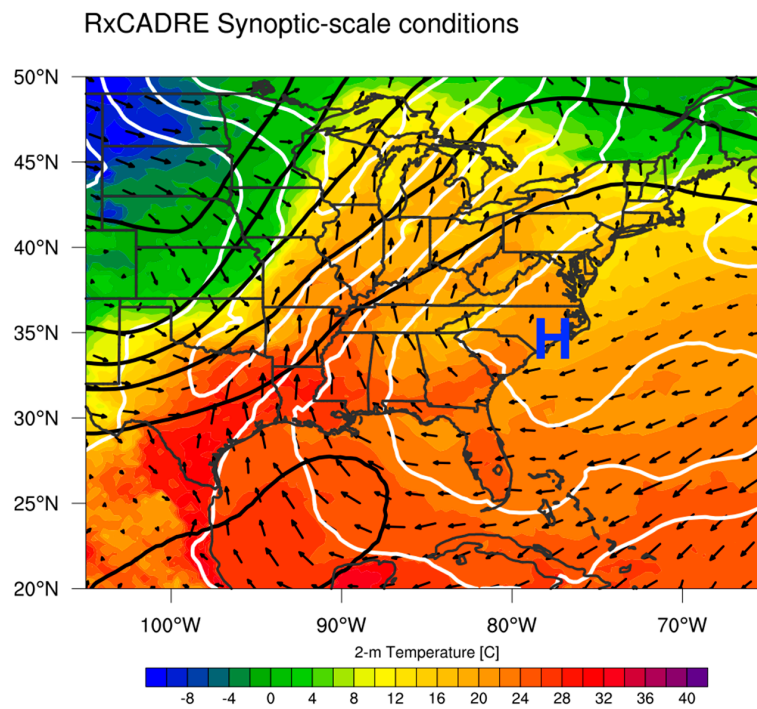


Figure 4. Synoptic-scale conditions during the L2F prescribed burn on 11 November 2012 at 1800 UTC. Wind vectors denote 10-m winds, white solid lines are 1000-hPa geopotential heights, and the black solid lines are 500-hPa geopotential heights.

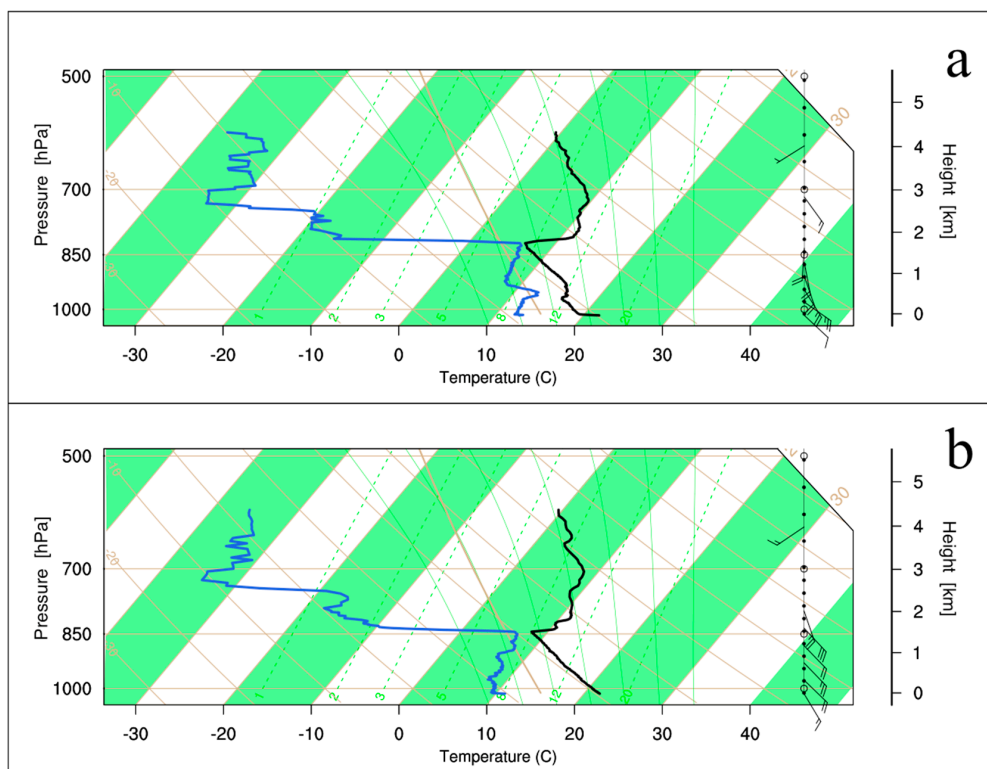


Figure 5. Skew-T diagram from radiosonde launches at Eglin Air Force base (a) prior to the L2F burn at 1525 UTC and (b) after the burn at 2149 UTC. The black line is air temperature (°C) while the blue line represents the dew point temperature (°C).

2.1. Measurements

2.1.1. Aircraft-Based Smoke Concentration Measurements

Downwind smoke measurements were obtained from a twin-engine Cessna 337 outfitted with a Picarro Cavity Ring-Down Spectroscopy (CRDS) gas analyzer. Smoke and ambient air was sampled through a stainless steel inlet with a diameter of 1.27-cm that was located on the pilot window. The CRDS instrument measured concentrations of CO₂, CO, CH₄, and water vapor every 2-s. A number of horizontal transects and vertical profiles of smoke were sampled between the fire ignition time at 1804 UTC through the end of the burn at 2059 UTC (Figure 2b) with measurements being acquired as far as 25-km downwind from the fire.

2.1.2. Fire Emission Estimates

Fire emissions (E) during the L2F operational burn were estimated by taking the product of the area burned (A), the amount of fuel consumed during the burn (FLC), and the emission factor of the species of interest (EF):

$$E(k, t, i) = A(k, t) \times FLC(k, t) \times EF(k, t, i) \quad (1)$$

where, *k* is the location, *t* is time, and *i* is the species. Fuel loads in the L2F plot were measured before and after the operational burn in order to estimate FLC [28]. Uncertainties with fuel loads were estimated to be 18%. Fire emission factors for different chemical species were estimated using aircraft smoke measurements during the L2F prescribed burn [29,30]. Airborne FRP measurements were used to spatiotemporally distribute fuel consumption over time and location within 15-m × 15-m grid cells every 200–300-s. For consistency, emissions were linearly interpolated to a temporal resolution of 60-s. As a result, there was approximately 25,000 grid cells emitting smoke throughout the duration of the L2F prescribed burn. Total uncertainties for CO fire emissions during the L2F operational burn were approximated as ~28%. Lastly, fire heat fluxes for the L2F burn were estimated by multiplying the heat content of fuel (18.6 MJ·kg⁻¹) with FLC [31].

2.1.3. Meteorological Measurements

The L2F operational burn was instrumented with a 10-m micrometeorological tower located in the middle of the burn plot (Figure 3), which was outfitted with sonic anemometers mounted at 8.7 and 3.8-m and thermocouples at 9.1-m. A second, 6-m tower was deployed just outside of the L2F burn plot with sonic anemometers mounted at 5.8 and 2.0-m. A Campbell Scientific datalogger was used to record data collected by the towers [27]. The California State University–Mobile Atmospheric Profiling System (CSU–MAPS) was also deployed outside of the L2F burn plot, which consisted of a scanning Doppler lidar, microwave temperature and humidity profile, and surface weather station [27]. Two upper-air soundings were recorded by releasing radiosondes before and after the L2F burn at 1525 and 2149 UTC, respectively (30.58 N, −86.68 W).

2.2. Atmospheric Transport

To simulate the downwind transport of smoke during the RxCADRE field campaign, the Stochastic Time-Inverted Lagrangian Transport model (STILT) [32] was used. Previously, STILT has been applied towards regional-scale wildfire modeling applications [33] and other trace gas studies [34], in addition to evaluating the performance of emission inventories using inverse modeling methods. Here, we used the STILT modeling framework to evaluate the performance of a frequently used plume rise model, for well-constrained cases where fire inputs are prescribed. Wind fields generated from the Advanced Research version of the Weather Research and Forecast model (WRF–ARW v3.4.1) [22] were used to drive STILT backward trajectories, while WRF-estimated environmental conditions for the L2F prescribed burn were used as boundary conditions for the plume rise model. A diagram of the smoke

modeling framework described here can be seen in Figure 6, with each modeling component described in further detail in Sections 2.2.1–2.2.3.

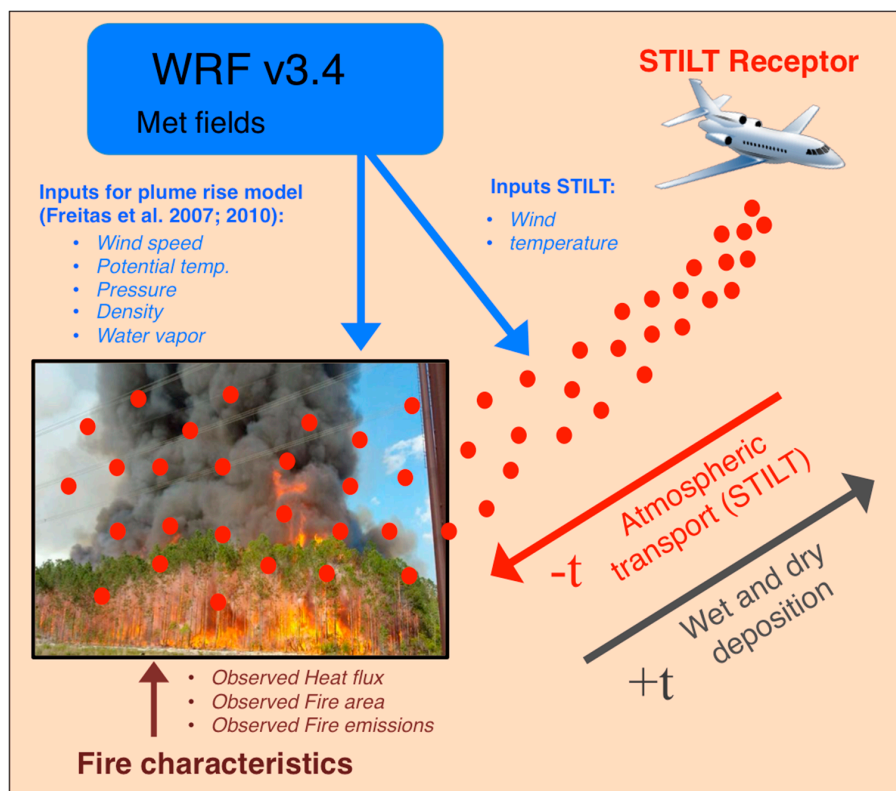


Figure 6. Schematic of the WRF–STILT (Stochastic Time-Inverted Lagrangian Transport) modeling framework used to model downwind smoke transport.

2.2.1. STILT Lagrangian Particle Dispersion Model

STILT is a time-reversed Lagrangian particle dispersion model that simulates atmospheric transport with an ensemble of backward trajectories released at a receptor location (receptor-oriented framework). STILT trajectories disperse over time as a result of turbulent motions that often characterize the PBL. In the case of STILT, subgrid-scale turbulence is parameterized as a Markov Chain [32]. Each STILT trajectory represents a parcel of air that has physical properties similar to that of the surrounding air, and is unaffected by gravitational settling or buoyancy.

Using the receptor-oriented framework, STILT can link changes in upwind emissions to concentration changes at the receptor via the footprint $f(x_r, t_r | x_i, y_j, t_m)$, where x_r and t_r denotes the receptor location and time, linked to some upwind source at location x_i, y_j at prior time t_m [32]:

$$f(x_r, t_r | x_i, y_j, t_m) = \frac{m_{\text{air}}}{h\bar{q}(x_i, y_j, t_m)} \frac{1}{N_{\text{tot}}} \sum_{p=1}^{N_{\text{tot}}} \Delta t_{p,i,j,k} \tag{2}$$

where m_{air} is defined as the molar mass of air (28.97 g mol^{-1}), and \bar{q} is average density of STILT trajectories below height h . N_{tot} is the total number of backward trajectories within the STILT ensemble, while $t_{p,i,j,k}$ is the amount of time that STILT trajectories spend below h at location x_i, y_j, t_m . In the case where no trajectories spend time below h at location x_i, y_j, t_m , the STILT footprint is assumed to be 0.

STILT simulations were performed for each aircraft measurement (every 2-s) starting on 11 November 2012 at 1743 and ending 3-h later at 2050 UTC (total of ~5500 simulations). Thus, each aircraft measurement at x_r and t_r was set as our STILT receptor. Each simulation consisted of

1000 backward trajectories with an output frequency of 1 min. Trajectories were terminated once they traveled 3 h backwards in time, generally after they have exited the RxCADRE domain. Here, we opted with backward trajectory simulations instead of the traditional approach of using forward trajectories as the number of active emission grid cells (~25,000) outnumbered the number of STILT receptors (~5500). As a result, the backward trajectory modeling approach was computationally cheaper by a factor of 5 relative to that of the forward trajectory modeling approach.

Because STILT was originally designed for regional-scale applications, several additional modifications were needed to make the STILT framework suitable for “hyper-local” modeling applications. First, STILT trajectories are only output at time steps ≥ 1 min. Since RxCADRE fire emissions are resolved at 15-m resolution, STILT backward trajectories were linearly interpolated in 3-dimensional space, every 1-s in an effort to prevent STILT trajectories from “jumping” over fire emission lines. Secondly, the original STILT footprint definition assumes that h in equation 2 is equal to 0.5 of the PBL height (z_i), and is insensitive to values that range from 0.1 to 1.0 as a result of STILT trajectories being well-dispersed through the depth of the PBL for regional-scale modeling applications [32]. For hyper-local modeling applications with time length-scales $< \sim 20$ min, this assumption is insufficient as STILT trajectories have not had enough time to disperse through the PBL. Following previous work [35], h was scaled as a time evolving Gaussian plume [36]. For cases where the width of the Gaussian plume (σ_w) is $< 0.5 z_i$, h was set equal to σ_w . When $\sigma_w > 0.5 z_i$, it is assumed that the STILT trajectories are sufficiently dispersed through the PBL so h was set to the default model definition of $h = 0.5 z_i$.

2.2.2. WRF

Wind fields generated from WRF were used to drive STILT backward trajectories (Figure 6). Custom time-averaged, mass-coupled velocity fields were used in an effort to improve mass conservation within the WRF–STILT modeling framework [37]. The WRF run for the L2F burn was initialized on 11 November 2012 at 0000 UTC using boundary conditions from the North American Mesoscale model (NAM). Initial boundary conditions were also derived from the NAM. The WRF simulation consisted of 4 nested domains with two-way nesting at 12-, 4-, 1.333-, and 0.444-km horizontal grid spacing (Figure 1), each with 42 vertical levels. Each of these domains was centered on Eglin Air Force Base, with the innermost domain covering all airborne smoke measurements, in addition to the prescribed burn plot located at 30.532 N and -86.721 W. For WRF physical parameterizations, we used the Rapid Radiative Transfer Model (RRTMG) for longwave and shortwave radiation [38], the NOAA land-surface model [39], the Grell–Devenyi ensemble scheme for a cumulus parameterization [40,41] for microphysics, and the Yonsei-University PBL scheme [42,43].

2.2.3. Plume Rise

The WRF simulation described above, provided only the mean winds not affected by the fire itself, and were not intended to resolve the plume dynamics. In an effort to model the fire plume rise associated with the L2F operational burn, we used a 1-D, cloud-resolving plume rise model by Freitas et al. [20], hereinafter referred to as the Freitas plume rise model. This model explicitly solves the equations for vertical momentum, first law of thermodynamics, and the continuity equation for water phases. The fire buoyancy is computed using the fire heat flux and fire area, with the heat flux being multiplied by a factor of 0.55 to convert it into a convective energy [44]. An underlying assumption with this plume rise model is that the plume geometry is treated as a homogeneous circle. This model also parameterizes entrainment, in addition to the drag generated as a result of environmental wind shear [45]. The Freitas plume rise model has been widely used by 3-D atmospheric and chemical transport models [46,47]. Atmospheric and chemical transport models often provide the plume rise model with ambient conditions of the atmosphere [25]. In turn, the plume rise model then provides a terminal injection height back to the 3-D host model, which can be used to determine the vertical level where emissions should be injected.

For this study, the ambient atmospheric conditions were derived from the WRF meteorological fields described in Section 2.2.2. Fire area and heat fluxes, which were used to drive the plume rise model, were obtained by multiplying the FLC with the heat content of fuel. For more details behind how this was calculated, please refer to Section 2.1.2. Finally, the terminal height of the plume was then provided to STILT to determine the injection level of the fire emissions. Plume rise heights were available every minute between 1810 and 2110 UTC.

3. Results

Aircraft transects during the L2F prescribed burn indicated a smoke plume oriented to the northwest as a result of prevailing winds out of the southeast (Figure 2). During each of the plume transects, CO enhancements, smoothed using a 20-s running mean, ranged from near zero to values exceeding >2000 ppb within the “corkscrew” flight profile at 1830–1835 UTC, where the aircraft ascended from an altitude of 120 to 1300-mASL at the center of the smoke plume within 3-km of the L2F burn plot (Figure 7). Measurements obtained from outside of the smoke plume were used as background and subtracted from the CO measurements taken from inside the plume to calculate CO enhancements from smoke.

CO measurements during the cork screw profile indicated a vertically homogenous smoke layer that extended from 120 to 1000-mASL, with the top of the smoke layer being measured at approximately 1100-m. Using classical dispersion theory [36] it is estimated that the plume top grew vertically by 150-m between the plume injection height over the fire to the aircraft measurement location 3.5-km downwind of fire. This suggests that the L2F prescribed burn had an estimated plume rise height of 950-m during the beginning of the prescribed burn.

In addition, three parking garage vertical profiles of the smoke plume were also initiated at 1815, 1933, 2005 UTC where the aircraft took 10-km long transects perpendicular to the long axis of the smoke plume (Figure 7). During each parking garage profile, smoke measurements were obtained at multiple levels ranging from 150 to 1200-mASL with CO smoke enhancements ranging from 0 to 900 ppb. For comparison against the observations from the L2F prescribed burn, we tested 4 different STILT model configurations, which varied the way that fire emissions were distributed vertically (Figure 8).

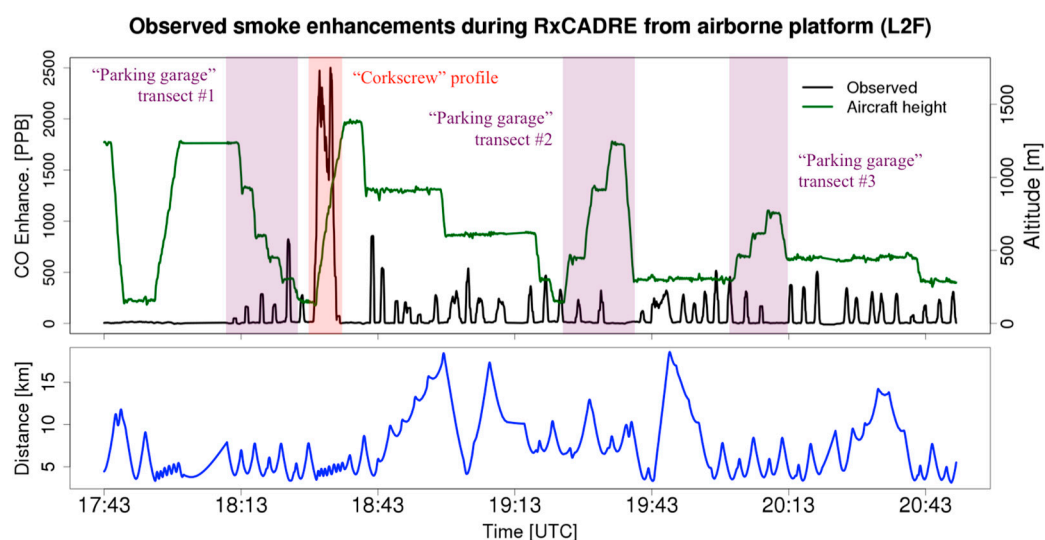


Figure 7. Aircraft measurements of CO enhancements above background during the L2F prescribed burn. Background concentrations were assumed to be ~110 ppb based on clean-air transects and were subtracted out. CO enhancements were smoothed using a 20-s centered moving average. The bottom panel indicates the aircraft distance from the middle of the L2F burn plot.

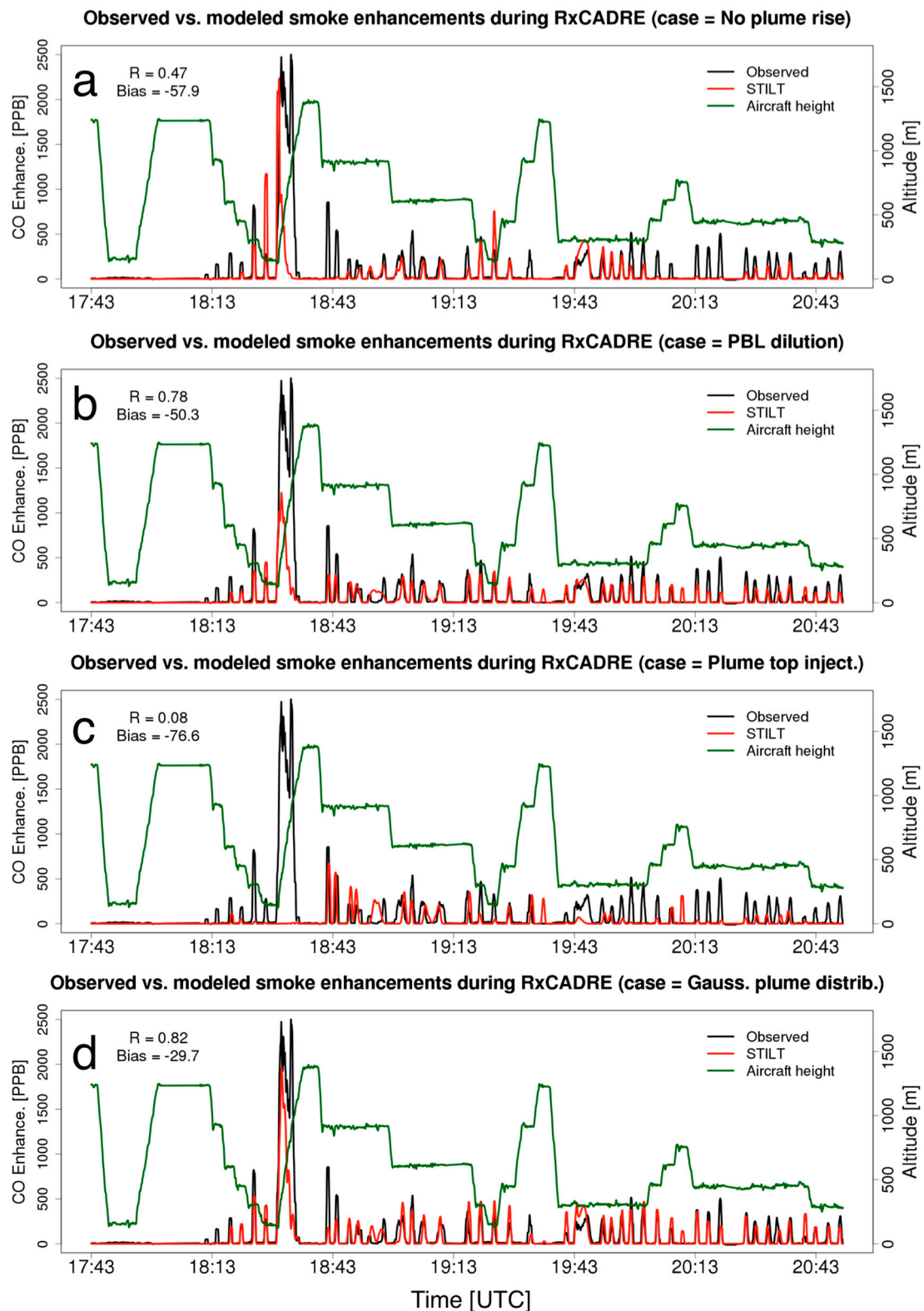


Figure 8. Modeled vs. observed CO enhancements during the L2F prescribed burn. Similar to Figure 9, the background CO concentrations (~110 ppb) were subtracted from the observed concentrations. Both modeled and observed CO enhancements were smoothed using a 20-s centered running average. (a) No plume rise, (b) PBL dilution, (c) plume-top, and (d) Gaussian plume rise configurations.

3.1. No Plume Rise Configuration

The first model configuration assumed that emissions were surface-based, thus no plume rise model was deployed. On average, the model did a reasonable job capturing the timing of CO enhancements along the majority of the smoke plume transects (Figure 8a). The model's ability to capture the timing of the smoke enhancements suggests that the smoke plume was correctly oriented horizontally, likely the result of the mean wind flow being accurately resolved by WRF throughout the duration of the L2F experiment. WRF wind comparisons to surface observations further confirm that wind direction errors were limited with a wind direction bias of -5° and a RMSE of 9° . Wind speed errors were also small, with a bias of 1.7 ms^{-1} and a RMSE of 1.8 ms^{-1} (not shown). While STILT did a sufficient job capturing the timing and location of smoke enhancements, it failed to accurately resolve the vertical distribution of smoke enhancements, which resulted in significant model errors throughout the duration of the L2F experiment ($r = 0.47$, bias = -57.9 ppb). The most significant errors were observed during the 3 parking garage transects. During these transects and profiles, STILT consistently underestimated CO enhancements aloft, while occasionally overestimating near-surface enhancements. Larger underestimations were also observed during the corkscrew transect, especially at higher-altitude measurement locations. Here, we suspect that the failure to include a plume rise model resulted in STILT's inability to accurately resolve the vertical distribution of smoke concentrations downwind of the L2F burn.

3.2. PBL Dilution Configuration

The second model configuration tested for the L2F experiment involved diluting fire emissions throughout the depth of the PBL, henceforth the PBL dilution configuration. While the correlation coefficient for this model setup was significantly improved ($r = 0.78$), resolving the vertical distribution of downwind smoke was still problematic (Figure 8b). Modeled smoke enhancements during the corkscrew transect were significantly underestimated at all altitudes (bias = -50.3 ppb). Furthermore, vertical distributions of smoke were also off during the 3 parking garage transects, although there seemed to be some improvement relative to the model configuration that assumed emissions were emitted strictly at the surface (Section 3.1). However, there were a number of large number of sampling periods during the L2F burn during which smoke was generally underestimated by the model: 1812–1845, 1955–2050. This general underestimation can likely be attributed to the fact that smoke was being diluted through a depth 1.25-km (Figure 9), when in reality, smoke was probably being vertically distributed throughout a much shallower layer, locally, as a result of the wildfire plume rise. It is worth mentioning that modeled underestimations were most pronounced for measurement periods that were close to the prescribed burn relative to locations that were further away (Figures 7 and 8b). By the time the smoke reached aircraft measurement locations further downwind $>10\text{-km}$, smoke emitted by the L2F burn were likely well-distributed throughout the PBL.

3.3. Plume-Top Configuration

Next, a model configuration that included the Freitas plume rise model was tested where all fire emissions were injected at the top of the plume, i.e., the plume-top configuration. During the L2F prescribed burn, plume rise heights were highest at the start of the burn, with an altitude of approximately 1000-m, with plume tops decreasing to a height of 600–700-mASL at the conclusion of the experiment (Figure 9). It is worth noting that while the average heat flux was highest near the start of the burn by a factor of 8, the decrease in plume heights were modest with a decline of only $\sim 20\%$. The limited change in the plume rise height can be explained by the area of active burning, which continued to increase throughout the L2F burn as the smoldering combustion and isolated pockets of flaming combustion persisted behind the flaming fire fronts. While the Freitas plume rise model is dependent on the fire heat flux, it also depends on the fire area, which is responsible for

determining the plume rise radius. The entrainment coefficient (ϵ_c) used within the Freitas model is defined as:

$$\epsilon_c = 2\alpha R^{-1} \quad (3)$$

where R is the radius of the plume and $\alpha = 0.1$ [20]. Thus, plume rises with a larger radius are less impacted by entrainment and can rise to a higher altitude [24].

RxCADRE (L2F) plume rise height estimated using the Freitas model

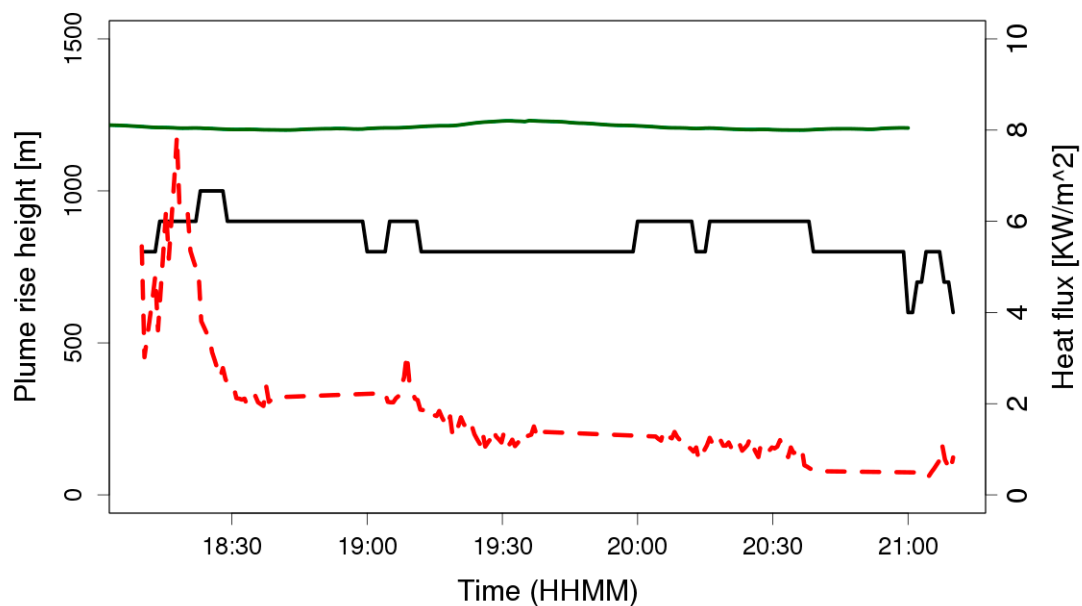


Figure 9. Time series of model-estimated plume rise heights (solid-black line), model-estimated planetary boundary layer (PBL) heights (solid-green line), and fire heat fluxes (red-dashed line) during the L2F prescribed burn.

Model estimated plume rises were in agreement with aircraft-derived plume rises at the beginning of the experiment, which suggested a maximum height around 950-m. For this model configuration, the surface-based footprint was redefined so that it could properly account for elevated emission sources, such as those associated with fires. Instead of assuming the default STILT footprint definition, which is bounded by the surface and $\frac{1}{2}$ PBL height, we calculated footprints every 200-m; starting from the surface to an altitude of 2000-m.

Simulations for the plume-top configuration were poor, with the model grossly underestimating CO enhancements at a number of transects (Figure 8c). CO enhancements at the start of the experiment were close to zero (1804–1843 UTC), suggesting that the modeled smoke plume was likely overshooting the aircraft measurement locations (1810–1835 UTC). After 1835 UTC, the model generally had issues resolving the vertical distribution of smoke, with CO enhancements being overestimated for higher altitude locations and underestimated for low altitude locations, especially during the 2nd and 3rd parking garage vertical profiles at 1933 and 2005 UTC. As a result, the correlation for this model configuration was particularly low ($r = 0.08$, bias = -76.6 ppb). The simulations here suggest that emitting smoke strictly at the plume top could be a poor assumption and potentially worse than assuming surface-based fire emissions.

3.4. Plume Rise + Gaussian Plume Configuration

For the last model configuration, fire emissions were distributed following a Gaussian distribution below the plume rise height, as suggested in a measurement-based plume study [48]. Overall, modeled results for this configuration were significantly improved, with the model accurately

resolving the location of smoke enhancements, in addition to the vertical distribution (Figure 8d). The vertical distribution of modeled CO enhancements during the 3 parking garage profiles were in good agreement with observations, with the model being able to replicate CO enhancements at most of the vertical transects. This was a significant improvement relative to the other simulations as seen in Figures 10 and 11 (parking garage profile #3), which either overestimated or underestimated enhancements aloft. However, similar to the other model configurations, the set up here also struggled with resolving CO enhancements during the corkscrew profile, with total enhancements underestimated by 50% when integrated throughout the column. It is suspected that the modeled plume centerline was not perfectly aligned with the observed plume during the corkscrew profile, resulting in underestimations in CO enhancements. Regardless, this configuration had CO enhancements elevated through 1000-mASL (Figures 12 and 13), which was a large improvement over the no plume rise (650-mASL) and plume-top configurations.

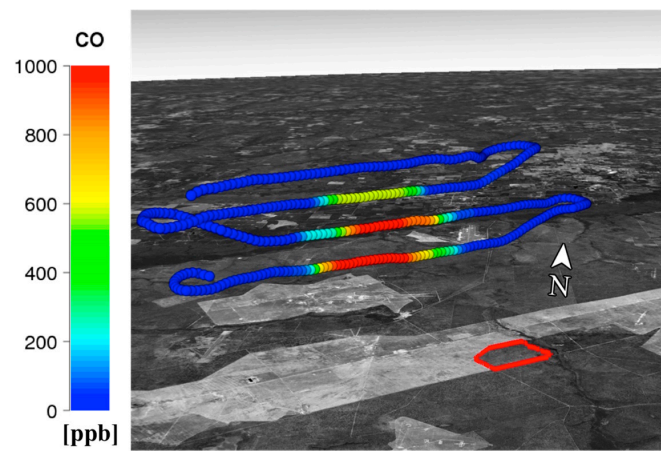


Figure 10. Observed CO enhancements during the parking garage #3 transect at 2035 UTC. Map data: Google, DigitalGlobe.

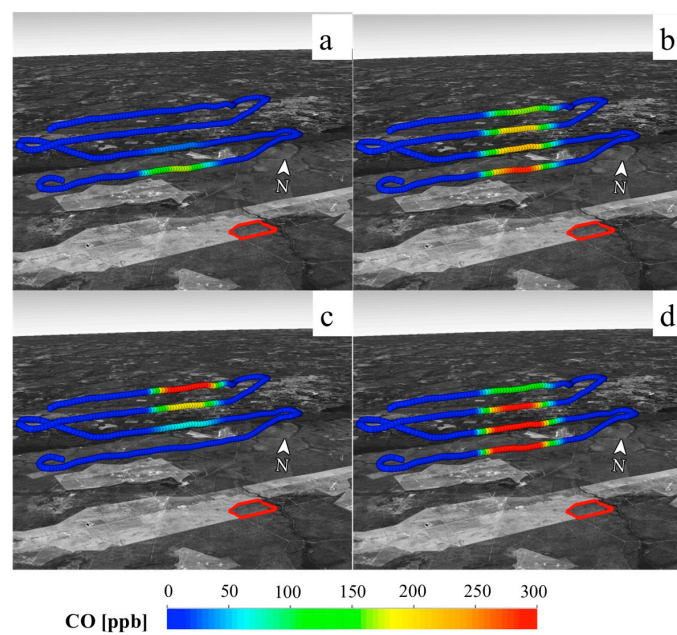


Figure 11. CO enhancements during the parking garage #3 transect at 2035 UTC for (a) no plume rise, (b) PBL dilution, (c) plume-top, and (d) Gaussian plume model configurations. The red polygon in the lower right corner of each panel indicates the L2F burn plot. Map data: Google, DigitalGlobe.

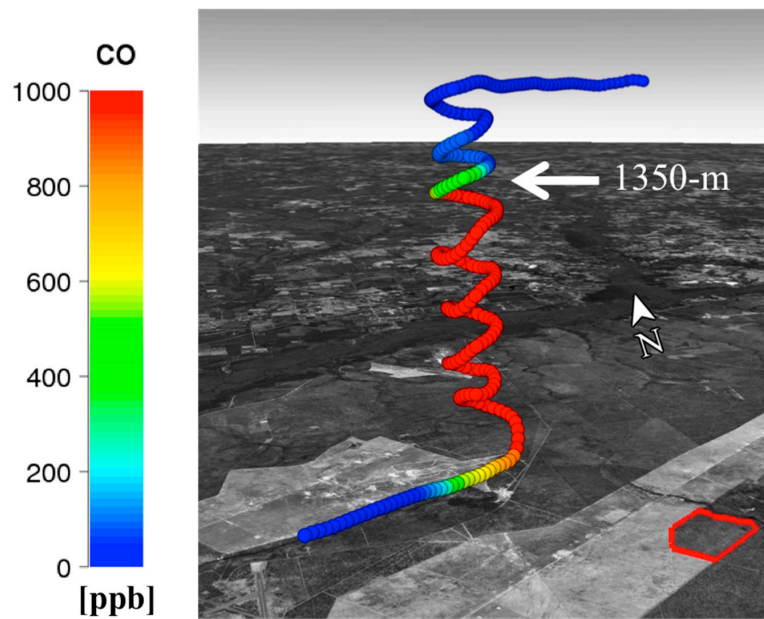


Figure 12. Same as Figure 10, but for the corkscrew vertical profile at 1830–1835 UTC. Map data: Google, DigitalGlobe.

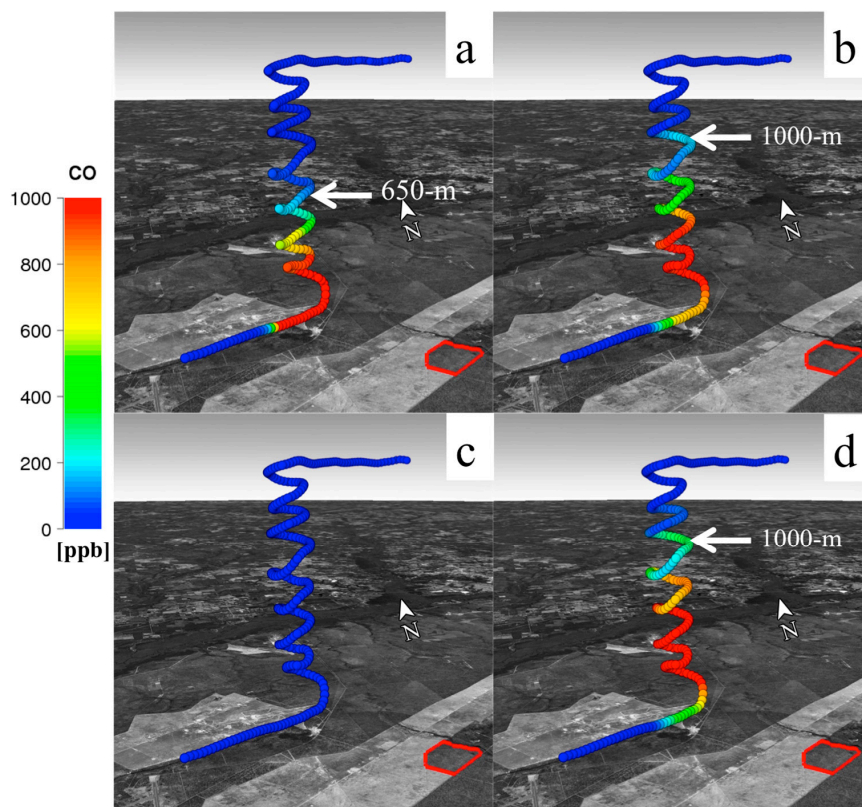


Figure 13. Same as Figure 11, but for the corkscrew vertical profile at 1830–1835 UTC. Map data: Google, DigitalGlobe.

It can be concluded that the plume rise + Gaussian configuration performed the best ($r = 0.82$) in regards to resolving the vertical distribution of smoke during the L2F prescribed burn while the surface-based and plume-top approaches were significantly worse. In addition, the bias for CO for this

configuration were the lowest (bias = -29.7 ppb). Furthermore, the results here suggest that resolving the vertical distribution of smoke emission is critical for local-scale smoke modeling applications.

4. Conclusions

Significant uncertainties exist within atmospheric and chemical transport models in regards to how fire emissions should be vertically distributed as a result of the wildfire plume rise. Fire area and heat flux are challenging parameters to measure, resulting in large errors that often propagate into plume rise parameterizations [11]. As a result, it is generally difficult to evaluate existing plume rise and smoke transport models, as there are a number of potential sources of errors. In an effort to reduce uncertainties associated with fire-input parameters such as fire area, heat flux, and emissions, a smoke modeling framework was applied to a well-constrained prescribed burn (RxCADRE). Here, a number of observations and measurements were taken in an effort to constrain fire emissions, fire area, and heat fluxes. In addition, downwind smoke concentrations were measured by an airborne platform, which took over 40 transects within 20-km of the L2F burn plot in an effort to resolve the spatiotemporal evolution of the smoke plume at local scales.

Four different model configurations were tested for this study, which included a set-up with (1) no fire plume rise, (2) emissions diluted throughout the depth of the PBL, (3) emissions injected at the plume-top, and (4) emissions distributed following a Gaussian profile below the top of the plume rise. Initial model results found that all the configurations, on average, were able to predict the orientation of the smoke plume, likely the result of the host meteorological model (WRF) accurately resolving the wind speed and direction throughout the duration of the L2F prescribed burn. However, results found that both the no plume rise and plume-top configurations were unable to predict the vertical distribution of smoke. The no plume rise configuration significantly underestimated higher-altitude smoke enhancements, while the plume-top scenario underestimated near-surface smoke enhancements. These results are consistent with another study, which also found that emitting smoke emissions within the surface layer did not compare well with observations [49]. The model configuration that diluted emissions throughout the depth of the PBL had no obvious biases with the vertical distribution of smoke outside of the fact that it generally underestimated smoke concentrations throughout the duration of the L2F experiment. It is worth noting that these underestimations were less pronounced when the aircraft was further away from prescribed burn, which is the likely result of smoke becoming convectively mixed throughout the PBL.

Results shown here suggest that injecting all fire emissions at the plume-top could be a worse assumption than prescribing surface-based emissions. The plume rise + Gaussian configuration performed the best, with no significant errors in regards to the vertical distribution of smoke. These results demonstrate that the incorporation of the fire plume rise is critical for resolving the vertical distribution of downwind smoke, particularly at local scales. Furthermore, comparisons between the plume-top and plume rise + Gaussian configurations reveal that the method used to vertically distribute fire emissions within the plume rise is also important.

From the results presented here, it is clear that at local scales, plume rises play a critical role in determining how smoke distributes downwind of the fire. It is recommended that plume rises be incorporated within models, with emissions being injected following a Gaussian-like profile. While the results here can provide guidance for atmosphere and chemical transport modelers, more work is needed to evaluate plume rises for well-observed case studies. In addition, more research is needed to determine the impact of wildfire plume rises on the long-range transport of smoke.

The RxCADRE L2F burn represents a small, well-contained prescribed burn, which may not necessarily be representative of a large, uncontrolled wildfire. The L2F burn was modest in size, involved light fuel loadings, and was ignited using multiple hand laid ignition lines. Prescribed fires that are larger in size, involve larger fuel loading, or employ aerial mass ignition may exhibit significantly different plume behavior. Finally, it should also be noted that prescribed burns under different meteorological conditions may significantly change the behavior of smoke plumes, thus it

is possible that the plume rise + Gaussian configuration recommended here may not always be the best set-up for different meteorological conditions. Thus, more studies and field experiments are likely needed that focus on wildfires instead of prescribe burns. An ideal case study would consist of fire input parameters that are well constrained via observations, along with downwind measurements of smoke profiles for large wildfires.

Author Contributions: Derek V. Mallia was responsible for the conception and design of the work presented in this manuscript. Derek was also responsible for writing the manuscript submitted here. In addition, model simulations performed here were set up and ran by Derek Mallia, with results being analyzed by the aforementioned author. Shawn Urbanski was responsible for providing aircraft data collected by the twin engine Cessna 337 which was outfitted with a Picarro Cavity Ring-Down Spectroscopy gas analyzer. Shawn also synthesized data during the RxCADRE L2F prescribed burn to generate fire emissions used for our model simulations. Adam Kochanski helped modify the plume rise model code so that it could work directly with output from the Weather Research and Forecast model. Finally, John Lin was responsible for providing the latest STILT model code, which was used to generate atmospheric transport simulations of smoke. Here, he also provided expertise for interpreting model results. In addition, John Lin was responsible for acquiring the funding needed to perform this study along with the providing the necessary computational resources for the model runs simulated here. All authors listed here had significant contributions in the form of manuscript revisions.

Acknowledgments: This study was made possible by funding from NOAA grant NA130AR4310087 and U.S. Forest Service grant 14-JV-11221637-027. The authors would like to thank Craig Clements, Steve Krueger, and John Horel for valuable input, and Georg Grell and Saulo Freitas for providing code for the Freitas plume rise model. The support and resources from the Center for High Performance Computing at the University of Utah are also gratefully acknowledged. The data used to produce the results in this study are available from the corresponding author upon request.

Conflicts of Interest: The authors declare no conflict of interest.

References

1. Galanter, M.; Levy, H.; Carmichael, G.R. Impacts of biomass burning on tropospheric CO, NO_x, and O₃. *J. Geophys. Res.* **2010**, *105*, 6633–6653. [[CrossRef](#)]
2. Intergovernmental Panel on Climate Change (IPCC). Contribution of Working Group I to the Fifth Assessment Report of the Intergovernmental Panel on Climate Change. In *Climate Change 2013: The Physical Science Basis*; Stocker, T.F., Qin, D., Plattner, G.-K., Tignor, M., Allen, S.K., Boschung, J., Nauels, A., Xia, Y., Bex, V., Midgley, P.M., Eds.; Cambridge University Press: Cambridge, UK, 2013; p. 1535.
3. Ramanathan, V.; Carmichael, G. Global and regional climate changes due to black carbon. *Nat. Geosci.* **2008**, *1*, 221–227. [[CrossRef](#)]
4. Bowman, M.J.S.; Balch, J.K.; Artaxo, P.; Bond, W.J.; Carlson, J.M.; Cochrane, M.A.; D'Antonio, C.M.; DeFries, R.S.; Doyle, J.C.; Harrison, S.P.; et al. Fire in the earth system. *Science* **2009**, *324*, 481–484. [[CrossRef](#)] [[PubMed](#)]
5. Lee, L.A.; Reddington, C.L.; Carslaw, K.S. On the relationship between aerosol model uncertainty and radiative forcing uncertainty. *Proc. Natl. Acad. Sci. USA* **2016**, *113*, 5820–5827. [[CrossRef](#)] [[PubMed](#)]
6. Sapkota, A.; Symons, J.M.; Kleissl, J.; Wang, L.; Parlange, M.B.; Ondov, J.; Breyssse, P.N.; Diette, G.B.; Eggleston, P.A.; Buckley, T. Impacts of the 2002 Canadian forest fires on particulate matter air quality in Baltimore City. *Environ. Sci. Technol.* **2005**, *39*, 24–32. [[CrossRef](#)] [[PubMed](#)]
7. Westerling, A.L.; Cayan, D.R.; Swetnam, T.W. Warming and earlier spring increase western U.S. forest wildfire activity. *Science* **2006**, *313*, 940–943. [[CrossRef](#)] [[PubMed](#)]
8. Spracklen, D.V.; Mickley, L.J.; Logan, J.A.; Hudman, R.C.; Yevich, R.; Flannigan, M.D.; Westerling, A.L. Impacts of climate change from 2000 to 2050 on wildfire activity and carbonaceous aerosol concentrations in the western United States. *J. Geophys. Res.* **2009**, *114*, D20301. [[CrossRef](#)]
9. Hurteau, M.D.; Westerling, A.L.; Wiedinmyer, C.; Bryant, B.P. Project effects of climate and development on California wildfire emissions through 2100. *Environ. Sci. Technol.* **2014**, *48*, 2298–2304. [[PubMed](#)]
10. Liu, C.L.; Mickley, L.J.; Sulprizio, M.P.; Dominici, F.; Yue, X.; Ebisu, K.; Anderson, G.B.; Khan, R.F.; Bravo, M.A.; Bell, M.L. Particulate air pollution from wildfires in the Western US under climate change. *Clim. Chang.* **2016**, *138*, 655–666. [[CrossRef](#)] [[PubMed](#)]
11. Val Martin, M.; Kahn, R.A.; Logan, J.A.; Paugam, R.; Wooster, M.; Ichoku, C. Space-based observational constraints for 1-D fire smoke plume rise models. *J. Geophys. Res.* **2012**, *117*, D22204. [[CrossRef](#)]

12. Fromm, M.; Bevilacqua, R.; Servranckx, R.; Rosen, J.; Thayer, J.P.; Herman, J.; Larko, D. Pyro-cumulonimbus injection of smoke to the stratosphere: Observations and impact of a super blowup in northwestern Canada on 3–4 August 1998. *J. Geophys. Res.* **2005**, *110*, D08205. [[CrossRef](#)]
13. Val Martin, M.; Logan, J.A.; Kahn, R.A.; Leung, F.Y.; Nelson, D.L.; Diner, D.J. Smoke injection heights from fires in North America: Analysis of 5 years of satellite observations. *Atmos. Chem. Phys.* **2010**, *10*, 1491–1510. [[CrossRef](#)]
14. Trentmann, J.; Andreae, M.O.; Graf, H.-F.; Hobbs, P.V.; Ottmar, R.D.; Trautmann, T. Simulation of a biomass-burning plume: Comparison of model results with observations. *J. Geophys. Res.* **2002**, *107*, 4013. [[CrossRef](#)]
15. Kahn, R.A.; Chen, Y.; Nelson, D.L.; Leung, F.-Y.; Li, Q.; Diner, D.J.; Logan, J.A. Wildfire smoke injection heights: Two perspectives from space. *Geophys. Res. Lett.* **2008**, *35*, L04809. [[CrossRef](#)]
16. Val Martin, M.; Honrath, R.; Owen, R.C.; Pfister, G.; Fialho, P.; Barata, F. Significant enhancements of nitrogen oxides, ozone and aerosol black carbon in the North Atlantic lower free troposphere resulting from North American boreal wildfires. *J. Geophys. Res.* **2006**, *111*, D23S60. [[CrossRef](#)]
17. Briggs, G.A. 1975: Plume rise predictions. In *Lectures on Air Pollution and Environmental Impact Analyses*; Haugen, D.A., Ed.; American Meteorological Society: Boston, MA, USA, 1975; pp. 59–111.
18. Liu, Y.; Achtemeier, G.L.; Goodrick, S.L.; Jackson, W.A. Important parameters for smoke plume rise simulation with Daysmoke. *Atmos. Pollut. Res.* **2010**, *1*, 250–259. [[CrossRef](#)]
19. Sofiev, M.; Ermakova, T.; Vankevich, R. Evaluation of the smoke-injection height from wild-land fires using remote-sensing data. *Atmos. Chem. Phys.* **2012**, *12*, 1995–2006. [[CrossRef](#)]
20. Freitas, S.R.; Longo, K.M.; Chatfield, R.; Latham, D.; Dias, M.A.F.S.; Andreae, M.O.; Prins, E.; Santos, J.C.; Gielow, R.; Carvalho, J.A., Jr. Including the sub-grid scale plume rise of vegetation fires in low resolution atmospheric transport models. *Atmos. Chem. Phys.* **2007**, *7*, 3385–3398. [[CrossRef](#)]
21. Mandel, J.; Beezley, J.D.; Kochanski, A.K. Coupled atmosphere-wildland fire modeling with WRF 3.3 and SFIRE 2011. *Geosci. Model Dev.* **2011**, *4*, 591–610. [[CrossRef](#)]
22. Skamarock, W.; Klemp, J.B.; Dudhia, J.; Gill, D.O.; Barker, D.M.; Wang, W.; Powers, J.G. A description of the Advanced Research WRF Version 3. *NCAR Tech. Note* **2008**, 126. [[CrossRef](#)]
23. Kochanski, A.K.; Jenkins, M.A.; Yedinak, K.; Mandel, J.; Beezley, J.; Lamb, B. Toward an integrated system for fire, smoke and air quality simulations. *Int. J. Wildland Fire* **2015**, *25*, 534–546. [[CrossRef](#)]
24. Raffuse, S.M.; Craig, K.J.; Larkin, N.K.; Strand, T.T.; Sullivan, D.C.; Wheeler, N.J.M.; Solomon, R. An Evaluation of Modeled Plume Injection Height with Satellite-Derived Observed Plume Height. *Atmosphere* **2012**, *3*, 103–123. [[CrossRef](#)]
25. Paugam, R.; Wooster, W.; Freitas, S.; Val Martin, M. A review of approaches to estimate wildfire plume injection height within large-scale atmospheric chemical transport models. *Atmos. Chem. Phys.* **2016**, *16*, 907–925. [[CrossRef](#)]
26. Ichoku, C.; Kahn, R.; Chin, M. Satellite contributions to the quantitative characterization of biomass burning for climate modeling. *Atmos. Res.* **2012**, *111*, 1–28. [[CrossRef](#)]
27. Clements, C.B.; Lareau, N.P.; Seto, D.; Contezac, J.; Davis, B.; Teske, C.; Zajkowski, T.J.; Hudak, A.T.; Bright, B.C.; Dickinson, M.B.; et al. Fire weather conditions and fire-atmosphere interactions observed during low-intensity prescribed fires—RxCADRE 2012. *Int. J. Wildland Fire* **2016**, *25*, 90–101. [[CrossRef](#)]
28. Ottmar, R.D.; Hudak, A.T.; Prichard, S.J.; Wright, C.S.; Restaino, J.C.; Kennedy, M.C.; Vihnanek, R.E. Pre-fire and post-fire surface fuel and cover measurements collected in the southeastern United States for model evaluation and development—RxCADRE 2008, 2011 and 2012. *Int. J. Wildland Fire* **2016**, *25*, 10–24. [[CrossRef](#)]
29. Strand, T.; Gullett, B.; Urbanski, S.; O’Neill, S.; Potter, B.; Aurell, J.; Holder, A.; Larkin, N.; Moore, M.; Rorig, M. Grassland and forest understorey biomass emissions from prescribed fires in the southeastern United States—RxCADRE 2012. *Int. J. Wildland Fire* **2016**, *25*, 102–113. [[CrossRef](#)]
30. Hudak, A.T.; Dickinson, M.B.; Bright, B.C.; Kremens, R.L.; Loudermilk, E.; O’Brian, J.J.; Hornsby, B.S.; Ottmar, R.D. Measurements relating to fire radiative energy density and surface fuel consumption—RxCADRE 2011 and 2012. *Int. J. Wildland Fire* **2016**, *25*, 25–37. [[CrossRef](#)]
31. Susott, R.A.; De Groot, W.F.; Shafizadeh, F. Heat content of natural fuels. *J. Fire Flammabl.* **1975**, *6*, 311–325.
32. Lin, J.C.; Gerbig, C.; Wofsy, S.C.; Andrews, A.E.; Daube, B.C.; Davis, K.J.; Grainger, C.A. A near-field tool for simulating the upstream influence of atmospheric observations: The Stochastic Time-Inverted Lagrangian Transport (STILT) model. *J. Geophys. Res.* **2003**, *108*, D003161. [[CrossRef](#)]

33. Mallia, D.V.; Lin, J.C.; Urbanski, S.; Ehleringer, J.; Nehr Korn, T. Impacts of upwind wildfire emissions on CO₂, CO₂, and PM_{2.5} concentrations in Salt Lake City, Utah. *J. Geophys. Res.* **2015**, *120*, 147–166. [[CrossRef](#)]
34. Lin, J.C.; Mallia, D.V.; Wu, D.; Stephens, B.B. How can mountaintop CO₂ observations be used to constrain regional carbon fluxes? *Atmos. Chem. Phys.* **2017**, *17*, 5561–5581. [[CrossRef](#)]
35. Fasoli, B.; Lin, J.C.; Bowling, D.R.; Mitchell, L.; Mendoza, D. Simulating atmospheric tracer concentrations for spatially distributed receptors: Updates to the Stochastic Time-Inverted Lagrangian Transport model's R interface (STILT-R version 2). *Geosci. Model Dev. Discuss.* **2018**. [[CrossRef](#)]
36. Taylor, G.I. Diffusion by continuous movements. *Phi. Trans.* **2015**, *215*, 523–537. [[CrossRef](#)]
37. Nehr Korn, T.; Eluszkiewicz, J.; Wofsy, S.C.; Lin, J.C.; Gerbig, C.; Longo, M.; Freitas, S. Coupled Weather Research and Forecasting-Stochastic Time-Inverted Lagrangian Transport (WRF-STILT) model. *Meteor. Atmos. Phys.* **2010**, *107*, 51–64. [[CrossRef](#)]
38. Iacono, M.J.; Delamere, J.S.; Mlawer, E.J.; Shephard, M.W.; Clough, S.A.; Collins, W.D. Radiative forcing by long-lived greenhouse gases: Calculations with the AER radiative transfer models. *J. Geophys. Res.* **2008**, *113*, D13103. [[CrossRef](#)]
39. Chen, F.; Dudhia, J. Coupling an advanced land-surface-hydrology model with the Penn State-NCAR MM5 modeling system. Part I: Model implementation and sensitivity. *Mon. Weather Rev.* **2001**, *129*, 569–586. [[CrossRef](#)]
40. Grell, G.A.; Devenyi, D. A generalized approach to parameterizing convection combining ensemble and data assimilation techniques. *Geophys. Res. Lett.* **2002**, *29*, 1693–1696. [[CrossRef](#)]
41. Lin, Y.-L.; Farley, F.D.; Orville, H.D. Bulk parameterization of the snow field in a cloud model. *J. Appl. Meteor.* **1983**, *22*, 1065–1092.
42. Mellor, G.L.; Yamada, T. Development of a turbulence closure model for geophysical fluid problems. *Rev. Geophys. Space Phys.* **1982**, *20*, 851–875. [[CrossRef](#)]
43. Hong, S.-Y.; Noh, Y.; Dudhia, J. A new vertical diffusion package with an explicit treatment of entrainment processes. *Mon. Weather Rev.* **2006**, *134*, 2318–2341. [[CrossRef](#)]
44. McCarter, R.J.; Broido, A. Radiative and convective energy from wood crib fires. *Pyrodynamics* **1965**, *2*, 65–85.
45. Freitas, S.R.; Longo, K.M.; Trentmann, J.; Latham, D. Technical note: Sensitivity of 1-D smoke plume rise models to the inclusion of environmental wind drag. *Atmos. Chem. Phys.* **2010**, *10*, 585–594. [[CrossRef](#)]
46. Grell, G.; Freitas, S.R.; Stuefer, M.; Fast, J. Inclusion of biomass burning in WRF-Chem: Impact of wildfires on weather forecasts. *Atmos. Chem. Phys.* **2011**, *11*, 5289–5303. [[CrossRef](#)]
47. Walter, C.; Freitas, S.R.; Kottmeier, C.; Kraut, I.; Rieger, D.; Vogal, H.; Vogal, B. The importance of plume rise on the concentrations and atmospheric impacts of biomass burning aerosol. *Atmos. Chem. Phys.* **2016**, *16*, 9201–9219. [[CrossRef](#)]
48. Lareau, N.P.; Clements, C. The mean and turbulent properties of a wildfire convective plume. *J. Appl. Meteor. Climatol.* **2017**, *56*, 2289–2299. [[CrossRef](#)]
49. Zhou, L.; Baker, K.R.; Napelenok, S.L.; Pouliot, G.; Elleman, R.; O'Neill, S.M.; Urbanski, S.P.; Wong, D.C. Modeling crop residue burning experiments to evaluate smoke emissions and plume transport. *Sci. Total Environ.* **2018**, *627*, 523–533. [[CrossRef](#)] [[PubMed](#)]

